

Linear Shape Deformation Models with Local Support Using Graph-based Structured Matrix Factorisation

Florian Bernard^{1,2} Peter Gemmar³ Frank Hertel¹ Jorge Goncalves² Johan Thunberg²

¹Centre Hospitalier de Luxembourg, Luxembourg

{bernard.florian,hertel.frank}@chl.lu

²Luxembourg Centre for Systems Biomedicine, University of Luxembourg, Luxembourg

{johan.thunberg,jorge.goncalves}@uni.lu

³Trier University of Applied Sciences, Trier, Germany

p.gemmar@hochschule-trier.de

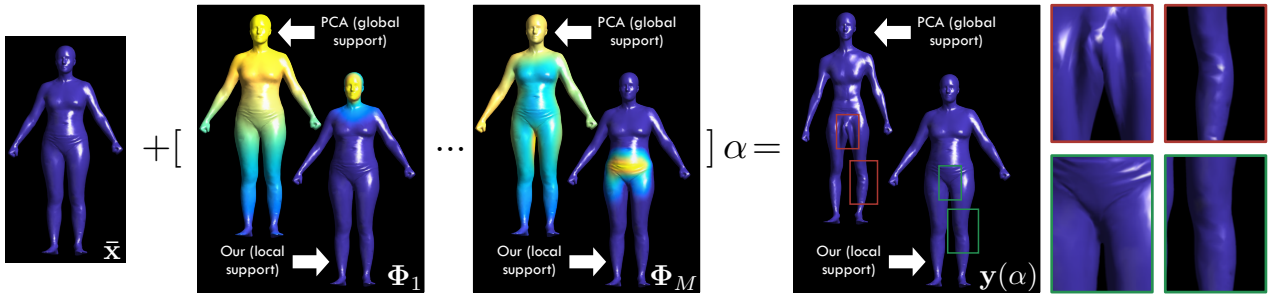


Figure 1. Global support factors of PCA lead to implausible body shapes, whereas the local support factors of our method give more realistic results. (Best viewed on screen when zoomed in)

Abstract

Representing 3D shape deformations by linear models in high-dimensional space has many applications in computer vision and medical imaging, such as shape-based interpolation or segmentation. Commonly, using Principal Components Analysis a low-dimensional (affine) subspace of the high-dimensional shape space is determined. However, the resulting factors (the most dominant eigenvectors of the covariance matrix) have global support, i.e. changing the coefficient of a single factor deforms the entire shape. In this paper, a method to obtain deformation factors with local support is presented. The benefits of such models include better flexibility and interpretability as well as the possibility of interactively deforming shapes locally. For that, based on a well-grounded theoretical motivation, we formulate a matrix factorisation problem employing sparsity and graph-based regularisation terms. We demonstrate that for brain shapes our method outperforms the state of the art in local support models with respect to generalisation ability and sparse shape reconstruction, whereas for human body shapes our method gives more realistic deformations.

1. Introduction

Due to their simplicity, linear models in high-dimensional space are frequently used for modelling non-linear deformations of shapes in 2D or 3D space. For example, Active Shape Models (ASM) [11], based on a statistical shape model, are popular for image segmentation. Usually, surface meshes, comprising faces and vertices, are employed for representing the surfaces of shapes in 3D. Dimensionality reduction techniques are then used to learn a low-dimensional representation of the vertex coordinates from training data. Frequently, an affine subspace that is sufficiently close to the training shapes is used. To be more specific, mesh deformations are modelled by expressing the vertex coordinates as the sum of a mean shape $\bar{\mathbf{x}}$ and a linear combination of M modes of variation $\Phi = [\Phi_1, \dots, \Phi_M]$, according to a weight/coefficient vector α , i.e. the vertices deformed by α are given by $\mathbf{y}(\alpha) = \bar{\mathbf{x}} + \Phi\alpha$, see Fig. 1. Commonly, by using Principal Components Analysis (PCA), the modes of variation are set to the most dominant eigenvectors of the covariance matrix of training shapes. PCA-based models are computationally convenient due to the orthogonality of the eigenvectors of the (real and symmetric) covariance matrix. Furthermore, due

to the diagonalisation of the covariance matrix, an axis-aligned Gaussian distribution of the weight vectors of the training data is obtained. A problem of PCA-based models is that eigenvectors have *global support*, meaning that adjusting the weight of a single factor affects *all* vertices of the shape (Fig. 1).

Thus, in this work, instead of eigenvectors as modes of variation, we consider more general *factors* that have *local support*, where adjusting the weight of a single factor leads only to a spatially localised deformation of the shape (Fig. 1). The set of all factors can be seen as a dictionary in order to represent shapes by a linear combination of the factors. Benefits of factors with local support include more realistic deformations (cf. Fig. 1), better interpretability of the deformations (e.g. clinical interpretability in a medical context [27]), and the possibility of interactive local mesh deformations (e.g. editing animated mesh sequences in computer graphics [23], or enhanced flexibility for interactive 3D segmentation based on statistical shape models [3]).

1.1. PCA Variants

PCA is a non-convex problem that admits the efficient computation of the global optimum, e.g. by Singular Value Decomposition (SVD). However, the downside is that the incorporation of arbitrary (convex) regularisation terms is not possible due to the SVD-based solution. Therefore, incorporating regularisation terms into PCA is an active field of research and several variants have been presented: Graph-Laplacian PCA [19] obtains factors such that the components vary smoothly according to a given graph. Robust PCA [7] formulates PCA as a convex low-rank matrix factorisation problem, where the nuclear norm is used as convex relaxation of the matrix rank. A combination of both Graph-Laplacian PCA and Robust PCA has been presented in [26]. The Sparse PCA (SPCA) method [16, 38] obtains sparse factors. Structured Sparse PCA (SSPCA) [18] additionally imposes structure on the sparsity of the factors using group sparsity norms, such as the mixed ℓ_1/ℓ_2 norm.

1.2. Deformation Model Variants

In [20], the flexibility of shape models has been increased by using PCA-based factors in combination with a *per-vertex* weight vector, in contrast to a single weight vector that is used for all vertices. In [12, 34], it is shown that additional elasticity in the PCA-based model can be obtained by manipulation of the sample covariance matrix. Whilst both approaches increase the flexibility of the shape model, they result in global support factors.

In [27], SPCA is used to model the anatomical shape variation of the 2D outlines of the corpus callosum. In [32], 2D images of the cardiac ventricle were used to train an Active Appearance Model based on Independent Component Analysis (ICA) [17]. Other applications of ICA for statis-

tical shape models are presented in [29, 37] as well as in [8], where ICA is used for motion editing. The Orthomax method, where the PCA basis is determined first and then rotated such that it has a “simple” structure, is used in [28]. The major drawback of SPCA, ICA and Orthomax is that the spatial relation between vertices is completely ignored.

The Key Point Subspace Acceleration method based on Varimax, where a statistical subspace and key points are automatically identified from training data, is introduced in [21]. For mesh animation, in [31] the clusters of spatially close vertices are determined first by spectral clustering, and then PCA is applied for each vertex cluster, resulting in one sub-PCA model per cluster. This two-stage procedure has the problem, that, due to the independence of both stages, it is unclear whether the clustering is optimal with respect to the deformation model. Also, a blending procedure for the individual sub-PCA models is required. A similar approach of first manually segmenting body regions and then learning a PCA-based model has been presented in [36].

Neumann et al. have presented the *Sparse Localised Deformation Components* (SPLOCS) method for obtaining localised deformation modes from animated mesh sequences [23]. They use a matrix factorisation formulation using a weighted ℓ_1/ℓ_2 norm regulariser. Local support factors are obtained by explicitly modelling local support regions, which are in turn used to update the weights of the ℓ_1/ℓ_2 norm *in each iteration*. This makes the non-convex optimisation problem even harder to solve and dismisses convergence guarantees. With that, a suboptimal initialisation of the support regions, as it is presented in their work, affects the quality of the found solution.

In the *compressed manifold modes* method [22], local support basis functions of the (discretised) Laplace-Beltrami operator of a *single* input mesh are determined.

1.3. Aims and Main Contributions

The work presented in this paper has the objective of learning local support deformation factors from training data. The main application of the resulting shape model is recognition, segmentation and shape interpolation [3]. Whilst our work remedies several of the mentioned shortcomings of existing methods, it can also be seen as complementary to SPLOCS, which is more tailored towards artistic editing and mesh animation. The most significant difference to SPLOCS is that we aim at letting the training shapes *automatically determine the location and size* of each local support region, which is advantageous for our applications in mind. This is achieved by formulating a matrix factorisation problem that incorporates regularisation terms which simultaneously account for *sparsity* and *smoothness* of the factors, where the graph-based smoothness regulariser accounts for smoothly varying neighbour vertices. In contrast to SPLOCS or sub-PCA, this results in an implicit cluster-

ing that is part of the optimisation and does *not require* an *initialisation* of local support regions, which in turn simplifies the optimisation procedure. Moreover, by integrating a *smoothness prior* into our framework we can *handle small training datasets*, even if the desired number of factors exceeds the number of training shapes. Our optimisation problem is formulated in terms of the Structured Low-Rank Matrix Factorisation framework [14], which has *appealing theoretical properties*.

2. Methods

First, we familiarise the reader with our notation and linear shape deformation models. Then, we state the objective and its formulation as optimisation problem, followed by the theoretical motivation. Finally, the block coordinate descent algorithm and the factor splitting method are presented.

2.1. Notation

\mathbf{I}_p denotes the $p \times p$ identity matrix, $\mathbf{1}_p$ the p -dimensional vector containing ones, $\mathbf{0}_{p \times q}$ the $p \times q$ zero matrix, and \mathbb{S}_p^+ the set of $p \times p$ positive semi-definite matrices. Let $\mathbf{A} \in \mathbb{R}^{p \times q}$. We use the notation $\mathbf{A}_{\mathcal{A}, \mathcal{B}}$ to denote the submatrix of \mathbf{A} with the rows indexed by the (ordered) index set \mathcal{A} and columns indexed by the (ordered) index set \mathcal{B} . The colon denotes the full (ordered) index set, e.g. $\mathbf{A}_{\mathcal{A}, :}$ is the matrix containing all rows of \mathbf{A} indexed by \mathcal{A} . For brevity, we may write \mathbf{A}_r to denote the p -dimensional vector formed by the r -th column of \mathbf{A} . The operator $\text{vec}(\mathbf{A})$ creates a pq -dimensional column vector from \mathbf{A} by stacking its columns, and \otimes denotes the Kronecker product.

2.2. Linear Shape Deformation Models

Let $\mathbf{X}_k \in \mathbb{R}^{N \times 3}$ be the matrix representation of a shape comprising N points (or vertices) in 3 dimensions, and let $\{\mathbf{X}_k : 1 \leq k \leq K\}$ be the set of K training shapes. In order to process multiple shapes in a meaningful way it is essential that the rows in each \mathbf{X}_k correspond to homologous points, which we assume as given. By using the column vector notation $\mathbf{x}_k = \text{vec}(\mathbf{X}_k) \in \mathbb{R}^{3N}$, all \mathbf{x}_k can be arranged in the matrix $\mathbf{X} = [\mathbf{x}_1, \dots, \mathbf{x}_K] \in \mathbb{R}^{3N \times K}$. For brevity, we assume that the mean shape $\bar{\mathbf{X}}$ has been subtracted from all shapes, such that $\sum_k \mathbf{X}_k = \mathbf{0}_{N \times 3}$, and that undesirable pose differences have been eliminated. \mathbf{X} is normalised such that the standard deviation of $\text{vec}(\mathbf{X})$ is one [23].

Pairwise relations between vertices are modelled by a weighted undirected graph $\mathcal{G} = (\mathcal{V}, \mathcal{E}, \omega)$ that is shared by all shapes. The node set $\mathcal{V} = \{1, \dots, N\}$ enumerates all N vertices, the edge set $\mathcal{E} \subseteq \{1, \dots, N\}^2$ represents the connectivity of the vertices, and $\omega \in \mathbb{R}_+^{|\mathcal{E}|}$ is the weight vector. The (scalar) weight ω_e of edge $e = (i, j) \in \mathcal{E}$ denotes the affinity between vertex i and j , where close vertices (in some appropriate sense) have high value ω_e . We assume there are

no self-edges, i.e. $(i, i) \notin \mathcal{E}$. Whilst in most applications the graph encodes pairwise *spatial* connectivity, affinities that are not of spatial nature are possible (e.g. symmetries, or prior anatomical knowledge in medical applications).

For the standard PCA-based method [11], the modes of variation in the M columns of the matrix $\Phi \in \mathbb{R}^{3N \times M}$ are defined as the M most dominant eigenvectors of the sample covariance matrix $\mathbf{C} = \frac{1}{K-1} \mathbf{X} \mathbf{X}^T$. However, we consider the generalisation where Φ contains general $3N$ -dimensional vectors, the *factors*, in its M columns. In both cases, the (linear) deformation model (modulo the mean shape) is given by

$$\mathbf{y}(\alpha) = \Phi \alpha, \quad (1)$$

with weight vector $\alpha \in \mathbb{R}^M$. Due to vectorisation, the rows with indices $\{1, \dots, N\}$, $\{N+1, \dots, 2N\}$ and $\{2N+1, \dots, 3N\}$ of \mathbf{y} (or Φ), correspond to the x , y and z components of the N vertices of the shape, respectively.

2.3. Objective and Optimisation Problem

Roughly spoken, the objective is to find $\Phi = [\Phi_1, \dots, \Phi_M]$ and $\mathbf{A} = [\alpha_1, \dots, \alpha_K] \in \mathbb{R}^{M \times K}$ for a given M such that, according to eq. (1), we can write

$$\mathbf{X} \approx \Phi \mathbf{A}, \quad (2)$$

where the factors Φ_m have *local support*. Local support means that Φ_m is sparse and that all *active* vertices, i.e. vertices that correspond to the non-zero elements of Φ_m , are connected by (sequences of) edges in the graph \mathcal{G} .

Now we state our problem formally as an optimisation problem. The theoretical motivation thereof is based on [2, 6, 14] and is recapitulated in section 2.4, where it will also become clear that our chosen regularisation term is related to the *Projective Tensor Norm* [2, 14].

A general matrix factorisation problem with squared Frobenius norm loss is given by

$$\min_{\Phi, \mathbf{A}} \|\mathbf{X} - \Phi \mathbf{A}\|_F^2 + \Omega(\Phi, \mathbf{A}), \quad (3)$$

where the regulariser Ω imposes certain properties upon Φ and \mathbf{A} . The optimisation is performed over *some* compact set (which we assume implicitly from here on). An obvious property of local support factors is sparsity. Moreover, it is desirable that in each factor components that are spatially close vary smoothly. Both properties together seem to be promising candidates to obtain local support factors, which we reflect in our regulariser. Our optimisation problem is given by

$$\min_{\substack{\Phi \in \mathbb{R}^{3N \times M} \\ \mathbf{A} \in \mathbb{R}^{M \times K}} \|\mathbf{X} - \Phi \mathbf{A}\|_F^2 + \lambda \sum_{m=1}^M \|\Phi_m\|_{\Phi} \|(\mathbf{A}_{m,:})^T\|_A, \quad (4)$$

where $\|\cdot\|_{\Phi}$ and $\|\cdot\|_A$ denote vector (semi-)norms. For

$\mathbf{z}' \in \mathbb{R}^K$, $\mathbf{z} \in \mathbb{R}^{3N}$, we define

$$\|\mathbf{z}'\|_A = \lambda_A \|\mathbf{z}'\|_2, \text{ and} \quad (5)$$

$$\|\mathbf{z}\|_\Phi = \lambda_1 \|\mathbf{z}\|_1 + \lambda_2 \|\mathbf{z}\|_2 + \lambda_\infty \|\mathbf{z}\|_{1,\infty}^{\mathcal{H}} + \lambda_G \|\mathbf{E}\mathbf{z}\|_2. \quad (6)$$

Both ℓ_2 norm terms will be discussed in section 2.4. The ℓ_1 norm is used to obtain sparsity in the factors. The (mixed) ℓ_1/ℓ_∞ norm is defined by

$$\|\mathbf{z}\|_{1,\infty}^{\mathcal{H}} = \sum_{g \in \mathcal{H}} \|\mathbf{z}_g\|_\infty, \quad (7)$$

where \mathbf{z}_g denotes a subvector of \mathbf{z} indexed by $g \in \mathcal{H}$. By using the collection $\mathcal{H} = \{\{i, i+N, i+2N\} : 1 \leq i \leq N\}$, a grouping of the x, y and z components per vertex is achieved, i.e. within a group g only the component with largest magnitude is penalised and no extra cost is to be paid for the other components being non-zero.

The last term in eq. (6), the graph-based ℓ_2 (semi-)norm, imposes smoothness upon each factor, such that neighbour elements according to the graph \mathcal{G} vary smoothly. Based on the incidence matrix of \mathcal{G} , we choose \mathbf{E} such that

$$\|\mathbf{E}\mathbf{z}\|_2 = \sqrt{\sum_{d \in \{0, N, 2N\}} \sum_{(i,j) \in e_p} \omega_{e_p} (\mathbf{z}_{d+i} - \mathbf{z}_{d+j})^2}. \quad (8)$$

As such, \mathbf{E} is a discrete (weighted) gradient operator and $\|\mathbf{E}\cdot\|_2^2$ corresponds to Graph-Laplacian regularisation [19]. \mathbf{E} is specified in the supplementary material.

2.4. Theoretical Motivation

For a matrix $\mathbf{X} \in \mathbb{R}^{3N \times K}$ and norms $\|\cdot\|_\Phi$ and $\|\cdot\|_A$, let us define the function

$$\psi^M(\mathbf{X}) = \min_{\substack{\{\Phi \in \mathbb{R}^{3N \times M}, \\ \mathbf{A} \in \mathbb{R}^{M \times K}\}: \\ \Phi \mathbf{A} = \mathbf{X}}} \sum_{m=1}^M \|\Phi_m\|_\Phi \|(\mathbf{A}_{m,\cdot})^T\|_A. \quad (9)$$

The function $\psi(\cdot) = \lim_{M \rightarrow \infty} \psi^M(\cdot)$ defines a norm known as *Projective Tensor Norm* or *Decomposition Norm* [2, 14].

Lemma 1. *For any $\epsilon > 0$ there exists an $M(\epsilon) \in \mathbb{N}$ such that $\|\psi(\mathbf{X}) - \psi^{M(\epsilon)}(\mathbf{X})\| < \epsilon$.*

Proof. For $\psi(\mathbf{X})$ there is a sequence $\{\Phi_i\}_{i=1}^\infty$ and a sequence $\{\mathbf{A}_i^T\}_{i=1}^\infty$ such that $\psi(\mathbf{X}) = \sum_{i=1}^\infty \|\Phi_i\|_\Phi \|\mathbf{A}_i^T\|_A$.

Let $l_m = \sum_{i=1}^m \|\Phi_i\|_\Phi \|\mathbf{A}_i^T\|_A$. The sequence l_m is monotone, bounded from above and convergent. Let $l_\infty = \psi(\mathbf{X})$ denote its limit. Since the sequence is convergent, there is $M(\epsilon)$ such that $\|l_\infty - l_j\| < \epsilon$ for $j \geq M(\epsilon)$. \square

We now proceed by introducing the optimisation problem

$$\min_{\mathbf{Z}} \|\mathbf{X} - \mathbf{Z}\|_F^2 + \lambda \psi^M(\mathbf{Z}). \quad (10)$$

Next, we establish a connection between Problem (10) and our problem (4). First, we assume that we are given a solution pair (Φ, \mathbf{A}) minimising Problem (4). By defining

$\mathbf{Z} = \Phi \mathbf{A}$, \mathbf{Z} is a solution to Problem (10). Secondly, assume we are given a solution \mathbf{Z} minimising Problem (10). To find a solution pair (Φ, \mathbf{A}) minimising Problem (4), one needs to compute the (Φ, \mathbf{A}) that achieves the minimum of the right-hand side of (9) for a given \mathbf{Z} .

This shows that given a solution to one of the problems, one can infer a solution to the other problem. Now we reformulate Problem (10) in order to numerically compute its solution. Define the matrices

$$\mathbf{Q} = \begin{bmatrix} \Phi \\ \mathbf{A}^T \end{bmatrix} \in \mathbb{R}^{3N+K \times M} \quad \text{and} \quad \mathbf{Y} = \mathbf{Q}\mathbf{Q}^T, \quad (11)$$

and the function $F : \mathbb{S}_{3N+K}^+ \rightarrow \mathbb{R}$ as

$$F(\mathbf{Y}) = F(\mathbf{Q}\mathbf{Q}^T) = \|\mathbf{X} - \Phi \mathbf{A}\|_F^2 + \lambda \psi^M(\Phi \mathbf{A}). \quad (12)$$

Let \mathbf{Y}^* denote a solution to the optimisation problem

$$\min_{\mathbf{Y} \in \mathbb{S}_{3N+K}^+} F(\mathbf{Y}). \quad (13)$$

For a given \mathbf{Y}^* , Problem (10) is minimised by the upper-right block matrix of \mathbf{Y}^* . The difference between (10) and (13) is that the latter is over the set of positive semi-definite matrices, which, at first sight, does not present any gain. However, under certain conditions, the global solution for \mathbf{Q} , rather than the product $\mathbf{Y} = \mathbf{Q}\mathbf{Q}^T$, can be obtained directly [6]. In [2] it is shown that if \mathbf{Q} is a *rank deficient* local minimum of $F(\mathbf{Q}\mathbf{Q}^T)$, then it is also a global minimum. Whilst these results only hold for twice differentiable functions F , Haeffele et al. have presented analogous results for the case of F being a sum of a twice-differentiable term and a non-differentiable term [14], such as ours above.

As such, *any* (rank deficient) local optimum of Problem (4) is also a global optimum. If in $\psi(\cdot)$, both $\|\cdot\|_\Phi$ and $\|\cdot\|_A$ are the ℓ_2 norm, $\psi(\cdot)$ is equivalent to the nuclear norm, commonly used as convex relaxation of the matrix rank [14, 25]. In order to steer the solution towards being rank deficient, we include ℓ_2 norm terms in $\|\cdot\|_\Phi$ and $\|\cdot\|_A$ (see (5) and (6)). With that, part of the regularisation term in (4) is the nuclear norm that accounts for low-rank solutions.

2.5. Block Coordinate Descent

A solution to problem (4) is found by block coordinate descent (BCD) [35] (Algorithm 1). It employs alternating proximal steps, which can be seen as generalisation of gradient steps for non-differentiable functions. Since computing the proximal mapping is repeated in each iteration, an efficient computation is essential. The proximal mapping of $\|\cdot\|_A$ in eq. (5) has a closed-form solution by *block soft thresholding* [24]. The proximal mapping of $\|\cdot\|_\Phi$ in eq. (6) is solved by dual forward-backward splitting [9, 10] (see supplementary material). The benefit of BCD is that it scales well to large problems. However, a downside is that by using the alternating updates one has only guaranteed convergence to a Nash equilibrium point [14, 35].

```

repeat
  // update  $\Phi$ 
   $\Phi' \leftarrow \Phi - \epsilon_\Phi \nabla_\Phi \|\mathbf{X} - \Phi \mathbf{A}\|_F^2$  // gradient step (loss)
  for  $m = 1, \dots, M$  do // proximal step  $\Phi$  (penalty)
    |  $\Phi_m \leftarrow \text{prox}_{\lambda \sum \|\cdot\|_\Phi \|(\mathbf{A}_{m,:})^T\|_A}(\Phi'_m)$ 
  // update  $\mathbf{A}$ 
   $\mathbf{A}' \leftarrow \mathbf{A} - \epsilon_A \nabla_A \|\mathbf{X} - \Phi \mathbf{A}\|_F^2$  // gradient step (loss)
  for  $m = 1, \dots, M$  do // proximal step  $\mathbf{A}$  (penalty)
    |  $\mathbf{A}_m \leftarrow \text{prox}_{\lambda \sum \|\Phi_m \cdot\|_\Phi \|\cdot\|_A}(\mathbf{A}'_m)$ 
until convergence

```

Algorithm 1: Simplified view of block coordinate descent. For details see [14, 35].

2.6. Factor Splitting

Whilst solving problem (4) leads to smooth and sparse factors, there is no guarantee that the factors have only a *single* local support region. In fact, due to the theoretical motivation in section 2.4, the solution of eq. (4) is steered towards being low-rank. However, the price to pay for a low-rank solution is that capturing multiple support regions in a *single* factor is preferred over having each support region in an individual factor (e.g. for $M = 2$ and any $\mathbf{a} \neq \mathbf{0}$, $\mathbf{b} \neq \mathbf{0}$, the matrix $\Phi = [\Phi_1 \Phi_2]$ has a lower rank when $\Phi_1 = [\mathbf{a}^T \ \mathbf{b}^T]^T$ and $\Phi_2 = \mathbf{0}$, compared to $\Phi_1 = [\mathbf{a}^T \ \mathbf{0}^T]^T$ and $\Phi_2 = [\mathbf{0}^T \ \mathbf{b}^T]^T$).

A simple yet effective way to deal with this issue is to split factors with multiple disconnected support regions into multiple (new) factors (see supplementary material). Since this is performed *after* the optimisation problem has been solved, it is preferable over pre- or intra-processing procedures [31, 23] since the optimisation remains unaffected and the data term in eq. (4) does not change due to the splitting.

3. Experimental Results

We compared the proposed method with *PCA* [11], *kernel PCA* (kPCA, cf. 3.2.2), *Varimax* [15], *ICA* [17], *SPCA* [18], *SSPCA* [18], and *SPLOCS* [23] on two real datasets, brain structures and human body shapes. Only our method and the SPLOCS method explicitly target to obtain local support factors, whereas the SPCA and SSPCA methods obtain sparse factors (for the latter the ℓ_1/ℓ_2 norm with groups defined by \mathcal{H} , cf. eq. (7), is used). The methods kPCA, SPCA, SSPCA, SPLOCS and ours require to set various parameters, which we address by random sampling over the parameter space (see supplementary material).

For all evaluated methods a factorisation $\Phi \mathbf{A}$ is obtained. W.l.o.g. we normalise the rows of \mathbf{A} to have standard deviation one (since $\Phi \mathbf{A} = (\frac{1}{s} \Phi)(s \mathbf{A})$ for $s \neq 0$). Then, the factors in Φ are ordered descendingly according to their ℓ_2 norms.

Next we describe the scores used to quantify *mesh reconstruction*, *generalisation*, *sparse reconstruction* and *specificity*.

3.1. Quantitative Measures

For $\mathbf{x} = \text{vec}(\mathbf{X})$ and $\tilde{\mathbf{x}} = \text{vec}(\tilde{\mathbf{X}})$, the *average error*

$$e_{\text{avg}}(\mathbf{x}, \tilde{\mathbf{x}}) = \frac{1}{N} \sum_{i=1}^N \|\mathbf{X}_{i,:} - \tilde{\mathbf{X}}_{i,:}\|_2 \quad (14)$$

and the *maximum error*

$$e_{\text{max}}(\mathbf{x}, \tilde{\mathbf{x}}) = \max_{i=1, \dots, N} \|\mathbf{X}_{i,:} - \tilde{\mathbf{X}}_{i,:}\|_2 \quad (15)$$

measure the agreement between shape \mathbf{X} and shape $\tilde{\mathbf{X}}$.

The *reconstruction error* for shape \mathbf{x}_k is measured by solving the overdetermined system $\Phi \alpha_k = \mathbf{x}_k$ for α_k in the least-squares sense, and then computing $e_{\text{avg}}(\mathbf{x}_k, \Phi \alpha_k)$ and $e_{\text{max}}(\mathbf{x}_k, \Phi \alpha_k)$, respectively.

To measure the *specificity error*, n_s shape samples are drawn randomly ($n_s=1000$ for the brain shapes and $n_s=100$ for the body shapes). For each drawn shape, the average and maximum errors between the closest shape in the training set are computed, which are denoted by s_{avg} and s_{max} , respectively. For simplicity, we assumed that the parameter vector α follows a zero mean Gaussian distribution, where the covariance matrix \mathbf{C}_α is estimated from the parameter vectors α_k of the K training shapes. With that, a random shape sample \mathbf{x}_r is generated by drawing a sample of the vector α_r from its distribution and setting $\mathbf{x}_r = \Phi \alpha_r$.

For evaluating the *generalisation error*, a collection of index sets $\mathcal{I} \subset 2^{\{1, \dots, K\}}$ is used, where each set $\mathcal{J} \in \mathcal{I}$ denotes the set of indices of the *test shapes* for one run and $|\mathcal{I}|$ is the number of runs. We used five-fold cross-validation, i.e. $|\mathcal{I}| = 5$ and each set \mathcal{J} contains $\text{round}(\frac{K}{5})$ random integers from $\{1, \dots, K\}$. In each run, the deformation factors $\Phi^{\mathcal{J}}$ are computed using the shapes with indices $\tilde{\mathcal{J}} = \{1, \dots, K\} \setminus \mathcal{J}$ as training data. For all test shapes \mathbf{x}_j , where $j \in \mathcal{J}$, the parameter vector α_j is determined by solving $\Phi^{\mathcal{J}} \alpha_j = \mathbf{x}_j$ in the least-squares sense. Eventually, the average reconstruction error $e_{\text{avg}}(\mathbf{x}_j, \Phi^{\mathcal{J}} \alpha_j)$ and the maximum reconstruction error $e_{\text{max}}(\mathbf{x}_j, \Phi^{\mathcal{J}} \alpha_j)$ are computed for each test shape, which we denote as g_{avg} and g_{max} , respectively. Moreover, the *sparse reconstruction errors* $g_{\text{avg}}^{0.05}$ and $g_{\text{max}}^{0.05}$ are computed in a similar manner, with the difference that α_j is now determined by using only 5% of the rows (selected randomly) of $\Phi^{\mathcal{J}}$ and \mathbf{x}_j , denoted by $\tilde{\Phi}^{\mathcal{J}}$ and $\tilde{\mathbf{x}}_j$. For that, we minimise $\|\tilde{\Phi}^{\mathcal{J}} \alpha_j - \tilde{\mathbf{x}}_j\|_2^2 + \|\Gamma \alpha_j\|_2^2$ with respect to α_j , which is a least-squares problem with Tikhonov regularisation, where Γ is obtained by Cholesky factorisation of $\mathbf{C}_\alpha = \Gamma^T \Gamma$. The purpose of this measure is to evaluate how well a deformation model interpolates an unseen shape from a small subset of its points, which is relevant for shape model-based surface interpolation [3].

3.2. Brain Structures

The first evaluated dataset comprises 8 (bilateral) brain structure meshes of $K=17$ subjects. All 8 meshes together have a total number of $N=1792$ vertices that are in correspondence among all 17 subjects. Moreover, all meshes have the same topology, i.e. seen as graphs they are isomorphic. A single deformation model is used to model the deformation of all 8 meshes in order to capture the interrelation between the brain structures. We fix the number of desired factors to $M=96$ to account for a sufficient amount of local details in the factors. Whilst the meshes are smooth and comparably simple in shape (cf. Fig. 3), a particular challenge is that the training dataset comprises only $K=17$ shapes.

3.2.1 Second-order Terms

Based on anatomical knowledge, we use the brain structure interrelation graph $\mathcal{G}_{bs} = (\mathcal{V}_{bs}, \mathcal{E}_{bs})$ shown in Fig. 2, where an edge between two structures denotes that a deformation of one structure may have a direct effect on the deformation of the other structure. Using \mathcal{G}_{bs} , we now build

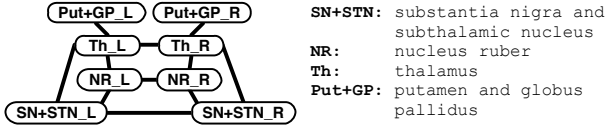


Figure 2. Brain structure interrelation graph.

a distance matrix that is then used in the SPLOCS method and our method. For $\sigma \in \mathcal{V}_{bs}$, let $g_\sigma \subset \{1, \dots, N\}$ denote the (ordered) indices of the vertices of brain structure σ . Let $\mathbf{D}_{\text{euc}} \in \mathbb{R}^{N \times N}$ be the Euclidean distance matrix, where $(\mathbf{D}_{\text{euc}})_{ij} = \|\bar{\mathbf{X}}_{i,\cdot} - \bar{\mathbf{X}}_{j,\cdot}\|_2$ is the Euclidean distance between vertex i and j of the mean shape $\bar{\mathbf{X}}$. Moreover, let $\mathbf{D}_{\text{geo}} \in \mathbb{R}^{N \times N}$ be the geodesic graph distance matrix of the mean shape $\bar{\mathbf{X}}$ using the graph induced by the (shared) mesh topology. By $\mathbf{D}_{\text{euc}}^\sigma \in \mathbb{R}^{|g_\sigma| \times |g_\sigma|}$ and $\mathbf{D}_{\text{geo}}^\sigma \in \mathbb{R}^{|g_\sigma| \times |g_\sigma|}$ we denote the Euclidean distance matrix and the geodesic distance matrix of brain structure σ , which are submatrices of \mathbf{D}_{euc} and \mathbf{D}_{geo} , respectively. Let \bar{d}^σ denote the average vertex distance between neighbour vertices of brain structure σ . We define the normalised geodesic graph distance matrix of brain structure σ by $\tilde{\mathbf{D}}_{\text{geo}}^\sigma = \frac{1}{\bar{d}^\sigma} \mathbf{D}_{\text{geo}}^\sigma$ and the matrix $\tilde{\mathbf{D}}_{\text{geo}} \in \mathbb{R}^{N \times N}$ is composed by the individual blocks $\tilde{\mathbf{D}}_{\text{geo}}^\sigma$.

The normalised distance matrix between structure σ and $\tilde{\sigma}$ is given by $\tilde{\mathbf{D}}_{\text{bs}}^{\sigma, \tilde{\sigma}} = \frac{2}{\bar{d}^\sigma + \bar{d}^{\tilde{\sigma}}} (\mathbf{D}_{\text{euc}})_{g_\sigma, g_{\tilde{\sigma}}} \in \mathbb{R}^{|g_\sigma| \times |g_{\tilde{\sigma}}|}$. The (symmetric) distance matrix $\tilde{\mathbf{D}}_{\text{bs}} \in \mathbb{R}^{N \times N}$ between all structures is constructed by

$$(\tilde{\mathbf{D}}_{\text{bs}})_{g_\sigma, g_{\tilde{\sigma}}} = \begin{cases} \tilde{\mathbf{D}}_{\text{bs}}^{\sigma, \tilde{\sigma}} & \text{if } (\sigma, \tilde{\sigma}) \in \mathcal{E}_{\text{bs}} \\ \mathbf{0}_{|g_\sigma| \times |g_{\tilde{\sigma}}|} & \text{else} \end{cases}. \quad (16)$$

For the SPLOCS method we used the distance matrix $\mathbf{D} = \alpha_D \tilde{\mathbf{D}}_{\text{geo}} + (1 - \alpha_D) \tilde{\mathbf{D}}_{\text{bs}}$. For our method, we construct the graph $\mathcal{G} = (\mathcal{V}, \mathcal{E}, \omega)$ (cf. section 2.2) by having an edge $e = (i, j)$ in \mathcal{E} for each $\omega_e = \alpha_D \exp(-(\tilde{\mathbf{D}}_{\text{geo}})_{i,j}^2) + (1 - \alpha_D) \exp(-(\tilde{\mathbf{D}}_{\text{bs}})_{i,j}^2)$ that is larger than the threshold θ . We used $\theta = 0.1$ to ignore edges with low weights in order to reduce the runtime of computing the proximal operator of $\|\cdot\|_\Phi$. In both cases we set $\alpha_D = 0.5$.

3.2.2 Dealing with the Small Training Set

For the PCA, Varimax and ICA methods the number of factors cannot be larger than K . For numerical reasons, when using the PCA and Varimax methods we set M such that 99.999% of the variance in the training data can be explained. Moreover, when we use our method, we eventually remove factors that are close to zero. The final number of factors M for each method is presented in Fig. 3.

For the used matrix factorisation framework it has been reported in [14] that setting M to a value larger than the expected rank of the solution but smaller than full rank has empirically led to good results. However, since our expected rank is $M = 96$ and the full rank is smaller than or equal to $K = 17$ this is not possible.

We deal with this issue by compensating the insufficient amount of training data by assuming smoothness of the deformations. Based on concepts introduced in [12, 33, 34], instead of the data matrix \mathbf{X} , we factorise a modified covariance matrix \mathbf{K} , which we refer to as *kernelised covariance matrix*. The standard PCA method finds the M most dominant eigenvectors of the covariance matrix \mathbf{C} by the (exact) factorisation $\mathbf{C} = \Phi \text{diag}(\lambda_1, \dots, \lambda_M) \Phi^T$. Using the kernelised covariance \mathbf{K} , one can incorporate additional elasticity into the resulting linear deformation model. For example, as shown in [34], using $\mathbf{K} = \mathbf{I}$ results in independent vertex movements. A more interesting approach is to combine the (scaled) covariance matrix with a smooth vertex deformation. We define $\mathbf{K} = \frac{1}{\|\text{vec}(\mathbf{X}\mathbf{X}^T)\|_\infty} \mathbf{X}\mathbf{X}^T + \mathbf{K}_{\text{euc}}$, with $\mathbf{K}_{\text{euc}} = \mathbf{I}_3 \otimes \mathbf{K}'_{\text{euc}} \in \mathbb{R}^{3N \times 3N}$. The matrix \mathbf{K}'_{euc} is given by the elements

$$(\mathbf{K}'_{\text{euc}})_{ij} = \exp\left(-\left(\frac{(\mathbf{D}_{\text{euc}})_{ij}}{2\beta \|\text{vec}(\mathbf{D}_{\text{euc}})\|_\infty}\right)^2\right), \quad (17)$$

where β is the bandwidth.

Setting Φ to the M most dominant eigenvectors of the symmetric and positive semi-definite [4] matrix \mathbf{K} gives the solution of *kernel PCA* (kPCA) [4]. In terms of our proposed matrix factorisation problem given in eq. (4), we find a factorisation $\Phi \tilde{\mathbf{A}}$ of \mathbf{K} , instead of factorising the data matrix \mathbf{X} . Since the regularisation term remains unchanged, the factor matrix Φ is still sparse and smooth (due to the norm $\|\cdot\|_\Phi$). Moreover, due to the nuclear norm term being contained in the product $\|\cdot\|_\Phi \|\cdot\|_A$ (cf. section 2.4), the re-

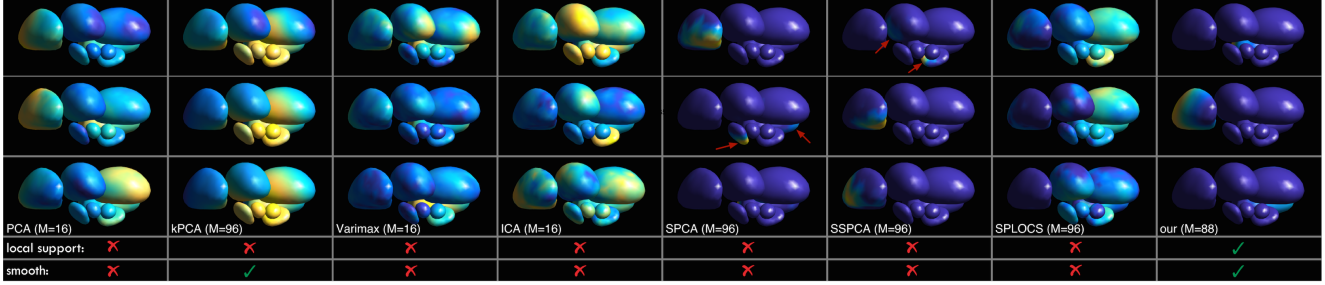


Figure 3. The colour-coded magnitude (blue corresponds to zero, yellow to the maximum deformation in each plot) for the three deformation factors with largest ℓ_2 norm is shown in the rows. The factors obtained by SPCA and SSPCA are sparse but not spatially localised (see red arrows). Our method is the only one that obtains local support factors. (Best viewed on screen when zoomed in)

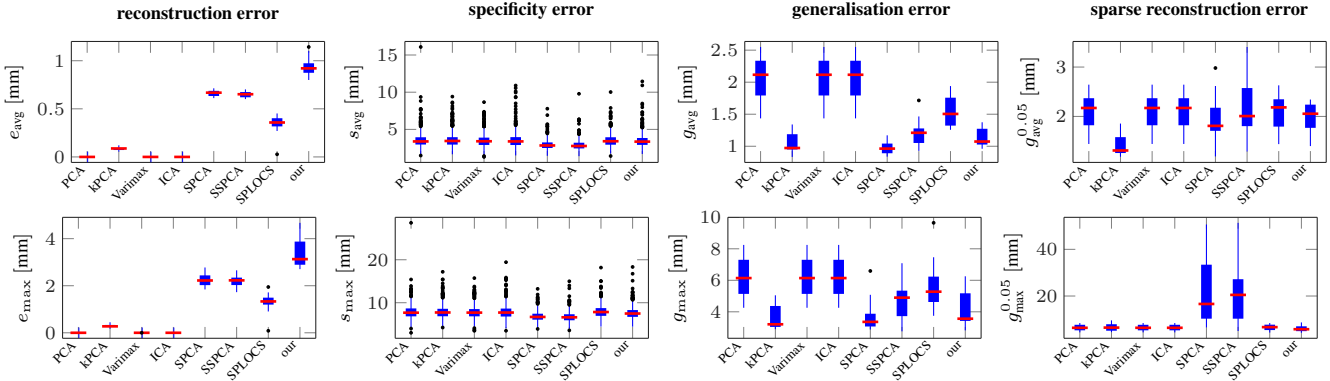


Figure 4. Boxplots of the considered quantitative measures for the brain shapes dataset. In each plot, the horizontal axis shows the individual methods and the vertical axis the error scores described in section 3.1. Compared to SPLOCS, which is the only other method explicitly striving for local support deformation factors, our method has a smaller generalisation error and sparse reconstruction error. The sparse but not spatially localised factors obtained by SPCA and SSPCA (cf. Fig. 3) result in a large maximum sparse reconstruction error (bottom right).

resulting factorisation $\tilde{\Phi}\tilde{\mathbf{A}}$ is steered towards being low-rank, in favour of the elaborations in section 2.4. However, the resulting matrix $\tilde{\mathbf{A}}$ now represents the weights for approximating the kernelised covariance \mathbf{K} by a linear combination of the columns of $\tilde{\Phi}$, rather than approximating the data matrix \mathbf{X} by a linear combination of the columns of $\tilde{\Phi}$. For the known $\tilde{\Phi}$, the weights that best approximate the *data matrix* \mathbf{X} are found by solving the linear system $\tilde{\Phi}\mathbf{A} = \mathbf{X}$ in the least-squares sense for \mathbf{A} .

3.2.3 Results

The magnitude of the deformation of the first three factors are shown in Fig. 3, where it can be seen that only SPCA, SSPCA, SPLOCS and our method obtain *sparse* deformation factors. The SPCA and SSPCA methods do not incorporate the spatial relation between vertices and as such the deformations are not spatially localised (see the red arrows in Fig. 3, where more than a single region is active). The factors obtained by the SPLOCS method are non-smooth and do not exhibit local support, in contrast to our method, where smooth deformation factors with local support are obtained.

The quantitative results presented in Fig. 4 reveal that

our method has a larger reconstruction error. This can be explained by the fact that due to the sparsity and smoothness of the deformation factors a very large number of basis vectors is required in order to exactly span the subspace of the training data. Instead, our method finds a simple (sparse and smooth) representation that explains the data approximately, in favour of Occam’s razor. Also, the average reconstruction error remains below 1mm, which is quite low considering that from left to right the brain structures span approximately 6cm. Considering specificity, all methods perform (roughly) in the same range. Looking at the generalisation score, it can be seen that PCA, Varimax and ICA, which have the lowest reconstruction errors, have the highest values regarding generalisation, which underlines that these methods overfit to the small training dataset. The kPCA method is able to overcome this issue due to the smoothness assumption. SPCA and SSPCA have good generalisation scores, however, these methods have a very high maximum reconstruction error, which can be seen in the bottom right in Fig. 4. Our method and SPLOCS are the only ones that explicitly strive for local support factors. Since our method outperforms SPLOCS with respect to generalisation and the reconstruction error, we claim that

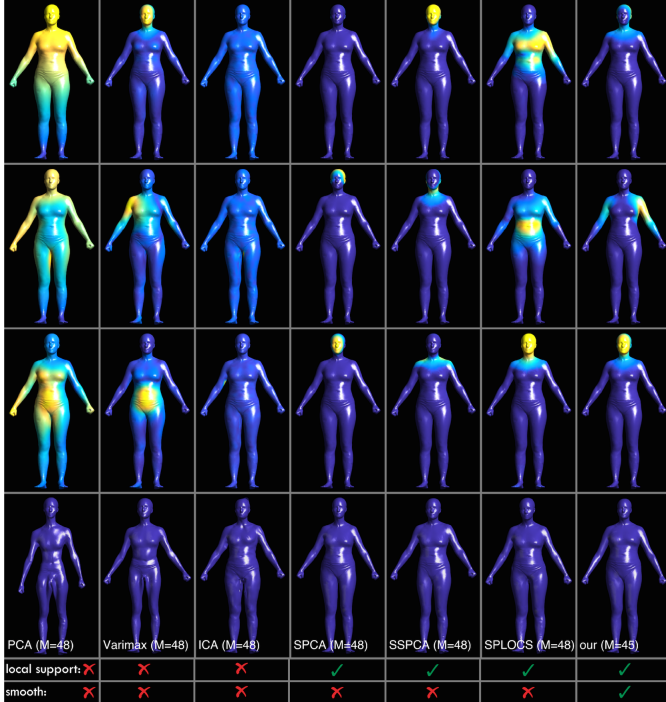


Figure 6. The visualisation of the deformation magnitudes show that the SPCA, SSPCA, SPLOCS and our method obtain local support factors (the second factor of our method has local support since the connection is at the back of the body shape). The bottom row depicts randomly drawn shape instances, where it can be seen that only the methods that obtain local support deformation factors result in plausible shapes. (Best viewed on screen when zoomed in)

our method outperforms the state of the art.

3.3. Human Body Shapes

Our second experiment is based on 1531 female human body shapes [36], where each shape comprises 12500 vertices that are in correspondence among the training set. Due to the large number of training data and the high level of details in the meshes (see Fig. 6), a kernelisation as done in section 3.2.2 is not used and we directly factorise the data matrix \mathbf{X} . The graph \mathcal{G} for our method is created in the same manner as for the brain shape dataset. The difference is that now $\tilde{\mathbf{D}}_{\text{geo}} = \frac{1}{\bar{d}} \mathbf{D}_{\text{geo}}$ is used to compute the edge weights, where \bar{d} denotes the average vertex distance between neighbour vertices and $\alpha_D = 1$.

3.3.1 Results

As shown in Fig. 5, quantitatively the evaluated methods have comparable performance, with the exception that ICA has worse overall performance. The most noticeable difference between the methods is the specificity error, where SPCA, SSPCA and our method perform best.

In Fig. 6 it can be seen that for SPCA, SSPCA, SPLOCS

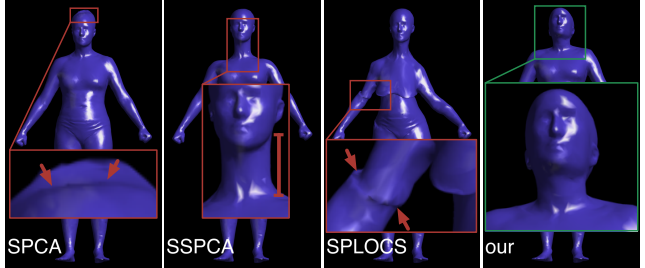


Figure 7. Shapes $\bar{\mathbf{x}} - 1.5\Phi_m$ for SPCA ($m=1$), SSPCA ($m=3$), SPLOCS ($m=1$) and our ($m=1$) method (cf. Fig. 6). Our method delivers the most realistic per-factor deformations. (Best viewed on screen when zoomed in)

and our method the deformation factors have local support. So it seems that for reasonably large datasets sparsity alone, as used in SPCA and SSPCA, is sufficient to account for local support factors. However, our method is the only one that explicitly strives for smoothness of the factors, which leads to more realistic human body deformations, as it is demonstrated in Fig. 7.

4. Conclusion

We presented a novel approach for learning a linear deformation model from training shapes, where the resulting factors exhibit local support. By embedding sparsity and smoothness regularisers into a theoretically well-grounded matrix factorisation framework, we model local support regions *implicitly*, and thus get rid of the initialisation of the size and location of local support regions, which so far has been necessary in existing methods. On the brain shapes dataset our method improves the state of the art with respect to generalisation and sparse reconstruction. For the body shapes dataset, quantitatively our method is on par with existing methods, whilst it delivers more realistic per-factor deformations. Since articulated motions violate our smoothness assumption, our method cannot handle them. However, when smooth deformations are a reasonable assumption, our method offers a higher flexibility and better interpretability compared to existing methods, whilst at the same time delivering more realistic deformations.

5. Acknowledgements

The authors would like to thank Yipin Yang and colleagues for making the human body shapes dataset publicly available. We also thank Benjamin D. Haeffele and René Vidal for providing their code.

We would also like to thank Thomas Bühler and Daniel Cremers for their helpful comments on the manuscript, as well as Luis Salamanca for helping to improve our figures.

The authors gratefully acknowledge the financial support by the Fonds National de la Recherche, Luxembourg (6538106, 8864515).

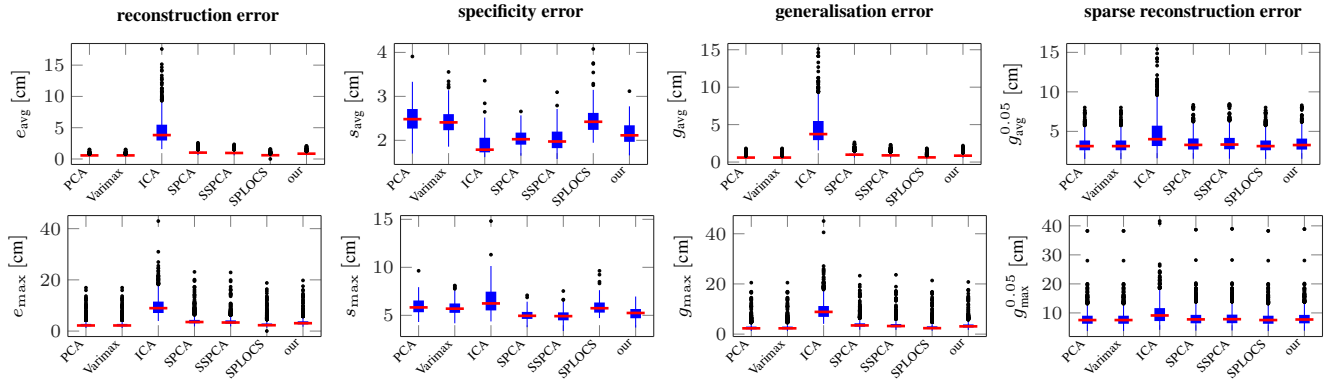


Figure 5. Boxplots of the considered quantitative measures in each column for the body shapes dataset. Quantitatively all methods have comparable performance, apart from ICA which performs worse.

References

- [1] F. Bach, R. Jenatton, J. Mairal, and G. Obozinski. Convex optimization with sparsity-inducing norms. *Optimization for Machine Learning*, pages 19–53, 2011. [11](#)
- [2] F. Bach, J. Mairal, and J. Ponce. Convex sparse matrix factorizations. *arXiv.org*, 2008. [3](#), [4](#)
- [3] F. Bernard, L. Salamanca, J. Thunberg, F. Hertel, J. Goncalves, and P. Gemmar. Shape-aware 3D Interpolation using Statistical Shape Models. In *Proceedings of Shape Symposium*, Delemont, Sept. 2015. [2](#), [5](#)
- [4] C. M. Bishop. *Pattern Recognition and Machine Learning (Information Science and Statistics)*. Springer-Verlag New York, Inc., Secaucus, NJ, USA, 2006. [6](#)
- [5] S. Boyd and L. Vandenberghe. *Convex Optimization*. Cambridge University Press, 2009. [12](#)
- [6] S. Burer and R. D. Monteiro. Local minima and convergence in low-rank semidefinite programming. *Mathematical Programming*, 103(3):427–444, 2005. [3](#), [4](#)
- [7] E. J. Candès, X. Li, Y. Ma, and J. Wright. Robust principal component analysis? *Journal of the ACM (JACM)*, 58(3):11, 2011. [2](#)
- [8] Y. Cao, A. Shapiro, P. Faloutsos, and F. Pighin. Motion editing with independent component analysis. *Visual Computer*, 2007. [2](#)
- [9] P. L. Combettes, D. Dũng, and B. C. Vũ. Dualization of signal recovery problems. *Set-Valued and Variational Analysis*, 18(3-4):373–404, 2010. [4](#), [11](#), [12](#)
- [10] P. L. Combettes and J.-C. Pesquet. Proximal splitting methods in signal processing. In *Fixed-point algorithms for inverse problems in science and engineering*, pages 185–212. Springer, 2011. [4](#), [11](#), [12](#)
- [11] T. F. Cootes and C. J. Taylor. Active Shape Models - Smart Snakes. In *In British Machine Vision Conference*, pages 266–275. Springer-Verlag, 1992. [1](#), [3](#), [5](#)
- [12] T. F. Cootes and C. J. Taylor. Combining point distribution models with shape models based on finite element analysis. *Image and Vision Computing*, 1995. [2](#), [6](#)
- [13] J. Duchi, S. Shalev-Shwartz, Y. Singer, and T. Chandra. Efficient projections onto the l_1 -ball for learning in high dimensions. In *Proceedings of the 25th international conference on Machine learning*, pages 272–279. ACM, 2008. [11](#)
- [14] B. Haeffele, E. Young, and R. Vidal. Structured low-rank matrix factorization: Optimality, algorithm, and applications to image processing. In *Proceedings of the 31st International Conference on Machine Learning (ICML-14)*, pages 2007–2015, 2014. [3](#), [4](#), [5](#), [6](#), [11](#)
- [15] H. H. Harman. *Modern factor analysis*. University of Chicago Press, 1976. [5](#)
- [16] M. Hein and T. Bühler. An inverse power method for nonlinear eigenproblems with applications in 1-spectral clustering and sparse PCA. In *Advances in Neural Information Processing Systems 23*, pages 847–855, 2010. [2](#)
- [17] A. Hyvärinen, J. Karhunen, and E. Oja. *Independent Component Analysis*. John Wiley & Sons, Apr. 2001. [2](#), [5](#)
- [18] R. Jenatton, G. Obozinski, and F. Bach. Structured sparse principal component analysis. *AISTATS*, 2009. [2](#), [5](#), [12](#)
- [19] B. Jiang, C. Ding, B. Luo, and J. Tang. Graph-Laplacian PCA: Closed-form solution and robustness. In *Computer Vision and Pattern Recognition (CVPR), 2013 IEEE Conference on*, pages 3492–3498. IEEE, 2013. [2](#), [4](#)
- [20] C. Last, S. Winkelbach, F. M. Wahl, K. W. Eichhorn, and F. Bootz. A locally deformable statistical shape model. In *Machine Learning in Medical Imaging*, pages 51–58. Springer, 2011. [2](#)
- [21] M. Meyer and J. Anderson. Key point subspace acceleration and soft caching. *ACM Transactions on Graphics (TOG)*, 26(3):74, 2007. [2](#)
- [22] T. Neumann, K. Varanasi, C. Theobalt, M. Magnor, and M. Wacker. Compressed manifold modes for mesh processing. In *Computer Graphics Forum*, pages 35–44. Wiley Online Library, 2014. [2](#)
- [23] T. Neumann, K. Varanasi, S. Wenger, M. Wacker, M. Magnor, and C. Theobalt. Sparse localized deformation components. *ACM Transactions on Graphics (TOG)*, 32(6):179, 2013. [2](#), [3](#), [5](#), [12](#)
- [24] N. Parikh and S. Boyd. Proximal algorithms. *Foundations and Trends in optimization*, 2013. [4](#), [11](#), [12](#)
- [25] B. Recht, M. Fazel, and P. A. Parrilo. Guaranteed minimum-rank solutions of linear matrix equations via nuclear norm minimization. *SIAM Review*, 52(3):471–501, 2010. [4](#)
- [26] N. Shahid, V. Kalofolias, X. Bresson, M. Bronstein, and P. Vandergheynst. Robust Principal Component Analysis on Graphs. *arXiv.org*, Apr. 2015. [2](#)

- [27] K. Sjostrand, E. Rostrup, C. Ryberg, R. Larsen, C. Studholme, H. Baezner, J. Ferro, F. Fazekas, L. Pantoni, D. Inzitari, and G. Waldemar. Sparse Decomposition and Modeling of Anatomical Shape Variation. *Medical Imaging, IEEE Transactions on*, 26(12):1625–1635, 2007. [2](#)
- [28] M. B. Stegmann, K. Sjöstrand, and R. Larsen. Sparse modeling of landmark and texture variability using the orthomax criterion. In *Medical Imaging*, pages 61441G–61441G. International Society for Optics and Photonics, 2006. [2](#)
- [29] A. Suinesiaputra, A. F. Frangi, M. Üzümcü, J. H. Reiber, and B. P. Lelieveldt. Extraction of myocardial contractility patterns from short-axes MR images using independent component analysis. In *Computer Vision and Mathematical Methods in Medical and Biomedical Image Analysis*, pages 75–86. Springer, 2004. [2](#)
- [30] R. Tarjan. Depth-first search and linear graph algorithms. *SIAM Journal on Computing*, 1(2):146–160, 1972. [12](#)
- [31] J. R. Tena, F. De la Torre, and I. Matthews. Interactive region-based linear 3d face models. *ACM Transactions on Graphics*, 2011. [2](#), [5](#)
- [32] M. Üzümcü, A. F. Frangi, M. Sonka, J. H. C. Reiber, and B. P. F. Lelieveldt. ICA vs. PCA Active Appearance Models: Application to Cardiac MR Segmentation. *MICCAI*, pages 451–458, 2003. [2](#)
- [33] Y. Wang and L. H. Staib. Boundary finding with correspondence using statistical shape models. In *IEEE Conference on Computer Vision and Pattern Recognition (CVPR)*, pages 338–345, 1998. [6](#)
- [34] Y. Wang and L. H. Staib. Boundary finding with prior shape and smoothness models. *Pattern Analysis and Machine Intelligence, IEEE Transactions on*, 22(7):738–743, 2000. [2](#), [6](#)
- [35] Y. Xu and W. Yin. A block coordinate descent method for regularized multiconvex optimization with applications to nonnegative tensor factorization and completion. *SIAM Journal on Imaging Sciences*, 6(3):1758–1789, 2013. [4](#), [5](#)
- [36] Y. Yang, Y. Yu, Y. Zhou, S. Du, J. Davis, and R. Yang. Semantic Parametric Reshaping of Human Body Models. In *Proceedings of the 2014 Second International Conference on 3D Vision-Volume 02*, pages 41–48. IEEE Computer Society, 2014. [2](#), [8](#)
- [37] R. Zewail, A. Elsafi, and N. Durdle. Wavelet-Based Independent Component Analysis For Statistical Shape Modeling. In *Canadian Conference on Electrical and Computer Engineering*, pages 1325–1328. IEEE, 2007. [2](#)
- [38] H. Zou, T. Hastie, and R. Tibshirani. Sparse principal component analysis. *Journal of Computational and Graphical Statistics*, 15(2):265–286, 2006. [2](#)

A. Supplementary Material

A.1. The matrix \mathbf{E} in eq. (8)

The matrix $\mathbf{E} \in \mathbb{R}^{3|\mathcal{E}| \times 3N}$ is defined as $\mathbf{E} = \mathbf{I}_3 \otimes \mathbf{E}'$, with $\mathbf{E}' \in \mathbb{R}^{|\mathcal{E}| \times N}$ being the weighted incidence matrix of the graph \mathcal{G} with elements

$$\mathbf{E}'_{pq} = \begin{cases} \sqrt{\omega_{e_p}} & \text{if } q = i \text{ for } e_p = (i, j) \\ -\sqrt{\omega_{e_p}} & \text{if } q = j \text{ for } e_p = (i, j) \\ 0 & \text{otherwise,} \end{cases} \quad (18)$$

where $e_p \in \mathcal{E}$ with $p = 1, \dots, |\mathcal{E}|$ denotes the p -th edge.

A.2. Proximal Operators

Definition 1. The proximal operator (or proximal mapping) $\text{prox}_{s\theta}(y) : \mathbb{R}^n \rightarrow \mathbb{R}^n$ of a function $\theta : \mathbb{R}^n \rightarrow \mathbb{R}$ scaled by $s > 0$ is defined by

$$\text{prox}_{s\theta}(y) = \arg \min_{\mathbf{x}} \left\{ \frac{1}{2s} \|\mathbf{x} - \mathbf{y}\|_2^2 + \theta(\mathbf{x}) \right\}. \quad (19)$$

A.2.1 Proximal Operator of $\|\cdot\|_A$

The proximal operator $\text{prox}_{\|\cdot\|_A}(\mathbf{y})$ of

$$\|\cdot\|_A = \lambda_A \|\cdot\|_2,$$

cf. eq. (5), can be computed by the so-called *block soft thresholding* [24], i.e.

$$\text{prox}_{s\|\cdot\|_2}(\mathbf{y}) = (1 - s/\|\mathbf{y}\|_2)_+ \mathbf{y}, \quad (20)$$

where for a vector $\mathbf{x} \in \mathbb{R}^p$, $(\mathbf{x})_+$ replaces each negative element in \mathbf{x} with 0. As such, a very efficient way for computing the proximal mapping of $\|\cdot\|_A$ is available.

A.2.2 Proximal Operator of $\|\cdot\|_\Phi$

The proximal mapping of

$$\|\cdot\|_\Phi = \lambda_1 \|\cdot\|_1 + \lambda_2 \|\cdot\|_2 + \lambda_\infty \|\cdot\|_{1,\infty}^{\mathcal{H}} + \lambda_{\mathcal{G}} \|\mathbf{E} \cdot\|_2,$$

cf. eq. (6), is given by

$$\begin{aligned} \text{prox}_{\|\cdot\|_\Phi}(\mathbf{z}) = \\ \arg \min_{\mathbf{x}} \left\{ \frac{1}{2} \|\mathbf{x} - \mathbf{z}\|_2^2 + \lambda_1 \|\mathbf{x}\|_1 + \lambda_2 \|\mathbf{x}\|_2 \right. \\ \left. + \lambda_\infty \|\mathbf{x}\|_{1,\infty}^{\mathcal{H}} + \lambda_{\mathcal{G}} \|\mathbf{E}\mathbf{x}\|_2 \right\}, \end{aligned} \quad (21)$$

which is a less trivial case, mainly because of the non-separability caused by the linear mapping \mathbf{E} inside the ℓ_2 norm. However, by introducing

$$f(\mathbf{x}) = \lambda_1 \|\mathbf{x}\|_1 + \lambda_2 \|\mathbf{x}\|_2 + \lambda_\infty \|\mathbf{x}\|_{1,\infty}^{\mathcal{H}} \quad (22)$$

and

$$g(\mathbf{x}) = \lambda_{\mathcal{G}} \|\mathbf{x}\|_2, \quad (23)$$

eq. (21) can be rewritten as

$$\arg \min_{\mathbf{x}} \left\{ \frac{1}{2} \|\mathbf{x} - \mathbf{z}\|_2^2 + f(\mathbf{x}) + g(\mathbf{E}\mathbf{x}) \right\}. \quad (24)$$

In this form, (24) can now be solved by a dual forward-backward splitting procedure [9, 10] as shown in Algorithm 2. Now the efficient computability hinges on the efficient computation of the (individual) proximal mappings of f and g .

Input: $\mathbf{z} \in \mathbb{R}^{3N}$

Output: $\mathbf{x} = \text{prox}_{\|\cdot\|_\Phi}(\mathbf{z})$

Parameters: $\lambda, \lambda_1, \lambda_\infty, \lambda_2, \lambda_{\mathcal{G}}$

Initialise: $\mathbf{v}, \epsilon \leftarrow 1e^{-4}, \gamma \leftarrow 1.999, \beta = \frac{1+\epsilon}{2}$

// Normalise \mathbf{E} (homogeneity of norm)

$\lambda_{\mathcal{G}} \leftarrow \lambda_{\mathcal{G}} \|\mathbf{E}\|_F; \quad \mathbf{E} \leftarrow \frac{\mathbf{E}}{\|\mathbf{E}\|_F}$

repeat

$\mathbf{x} \leftarrow \text{prox}_{\lambda_1 \|\cdot\|_1}(\mathbf{z} - \mathbf{E}^T \mathbf{v})$ // ℓ_1 prox, (25)

$\mathbf{x} \leftarrow \text{prox}_{\lambda_\infty \|\cdot\|_{1,\infty}^{\mathcal{H}}}(\mathbf{x})$ // ℓ_1/ℓ_∞ , [1, 13]

$\mathbf{x} \leftarrow \text{prox}_{\lambda_2 \|\cdot\|_2}(\mathbf{x})$ // ℓ_2 prox, (20)

$\mathbf{v} \leftarrow \mathbf{v} + \beta \gamma (\mathbf{E}\mathbf{x} - \text{prox}_{\lambda_{\mathcal{G}}/\gamma \|\cdot\|_2}(\frac{\mathbf{v} + \gamma \mathbf{E}\mathbf{x}}{\gamma}))$ // †

until convergence

Algorithm 2: Dual forward-backward splitting algorithm to compute the proximal mapping of $\|\cdot\|_\Phi$.

Since g is a (weighted) ℓ_2 norm, its proximal mapping is given by *block soft thresholding* presented in eq. (20).

In f , the sum of weighted ℓ_1 and ℓ_1/ℓ_∞ norms is an instance of the *sparse group lasso* and can be computed by applying the *soft thresholding* [24]

$$\text{prox}_{s\|\cdot\|_1}(\mathbf{y}) = (\mathbf{y} - s)_+ - (-\mathbf{y} - s)_+ \quad (25)$$

first, followed by *group soft thresholding* [1]. As shown in [14, Thm. 3], the ℓ_2 term can be additionally incorporated by composition, i.e. by subsequently applying *block soft thresholding* as presented in (20).

Now, for solving the *group soft thresholding* for the proximal mapping of the ℓ_1/ℓ_∞ norm, one can use the fact that for any norm ω with dual norm ω^* , $\text{prox}_{s\omega}(\mathbf{y}) = \mathbf{y} - \text{proj}_{\omega^* \leq s}(\mathbf{y})$, where $\text{proj}_{\omega^* \leq s}(\mathbf{y})$ is the projection of \mathbf{y} onto the ω^* norm ball with radius s [1]. The dual norm of the ℓ_1/ℓ_∞ norm, eq. (7), is the ℓ_∞/ℓ_1 norm

$$\|\mathbf{z}\|_{\infty,1}^{\mathcal{H}} = \max_{g \in \mathcal{H}} \|\mathbf{z}_g\|_1. \quad (26)$$

The orthogonal projection $\text{proj}_{\|\cdot\|_{\infty,1}^{\mathcal{H}} \leq s}$ onto the ℓ_∞/ℓ_1 ball is obtained by projecting separately each subvector \mathbf{z}_g onto the ℓ_1 ball in $\mathbb{R}^{|g|}$ [1], demanding an efficient projection onto the ℓ_1 norm ball. Due to the special structure of our groups in \mathcal{H} , i.e. there are exactly N non-overlapping groups, each of them comprising of three elements, a vectorised Matlab implementation of the method by Duchi et al. [13] can be employed.

Definition 2. (Convex Conjugate)

Let $\theta^*(\mathbf{y}) = \sup_{\mathbf{x}}(\mathbf{y}^T \mathbf{x} - \theta(\mathbf{x}))$ be the convex conjugate of θ .

The update of the dual variable \mathbf{v} in Algorithm 2 (see the line marked with †) is based on the update

$$\mathbf{v} \leftarrow \mathbf{v} + \beta(\text{prox}_{\gamma(\lambda_{\mathcal{G}}\|\cdot\|_2)^*}(\mathbf{v} + \gamma \mathbf{E}\mathbf{x}) - \mathbf{v}), \quad (27)$$

presented in [10, 9], where $(\cdot)^*$ denotes the convex conjugate.

Let us introduce some tools first.

Lemma 2. (Extended Moreau Decomposition) [24]

It holds that

$$\forall \mathbf{y} : \mathbf{y} = \text{prox}_{s\theta^*}(\mathbf{y}) + s \text{prox}_{\theta^*/s}(\mathbf{y}/s). \quad (28)$$

Lemma 3. (Conjugate of conjugate) [5]

For closed convex θ , it holds that $\theta^{**} = \theta$.

Corollary 1. For convex and closed θ , it holds that

$$\forall \mathbf{y} : \mathbf{y} = \text{prox}_{s\theta^*}(\mathbf{y}) + s \text{prox}_{\theta/s}(\mathbf{y}/s). \quad (29)$$

Proof. Define $\theta' = \theta^*$ and apply Lemma 2 and Lemma 3 with θ' in place of θ . \square

Since for our choice of $\theta = \lambda_{\mathcal{G}}\|\cdot\|_2$, θ is a closed convex function, by Corollary 1, one can write

$$\text{prox}_{\gamma(\lambda_{\mathcal{G}}\|\cdot\|_2)^*}(\mathbf{y}) = \mathbf{y} - \gamma \text{prox}_{\lambda_{\mathcal{G}}/\gamma\|\cdot\|_2}(\mathbf{y}/\gamma). \quad (30)$$

With that, the right-hand side of eq. (27) can be written as

$$\begin{aligned} & \mathbf{v} + \beta(\mathbf{v} + \gamma \mathbf{E}\mathbf{x} - \gamma \text{prox}_{\lambda_{\mathcal{G}}/\gamma\|\cdot\|_2}(\frac{\mathbf{v} + \gamma \mathbf{E}\mathbf{x}}{\gamma}) - \mathbf{v}) \\ &= \mathbf{v} + \beta(\gamma \mathbf{E}\mathbf{x} - \gamma \text{prox}_{\lambda_{\mathcal{G}}/\gamma\|\cdot\|_2}(\frac{\mathbf{v} + \gamma \mathbf{E}\mathbf{x}}{\gamma})) \\ &= \mathbf{v} + \beta\gamma(\mathbf{E}\mathbf{x} - \text{prox}_{\lambda_{\mathcal{G}}/\gamma\|\cdot\|_2}(\frac{\mathbf{v} + \gamma \mathbf{E}\mathbf{x}}{\gamma})). \end{aligned} \quad (31)$$

A.3. Factor Splitting

The *factor splitting* procedure is presented in Algorithm 3.

```

Input: factor  $\phi \in \mathbb{R}^{N \times 3}$  where  $\text{vec}(\phi) = \Phi_m$ , graph  $\mathcal{G} = (\mathcal{V}, \mathcal{E})$ 
Output:  $J$  factors  $\Phi' \in \mathbb{R}^{3N \times J}$  with local support
Initialise:  $\mathcal{E}' = \emptyset$ ,  $\Phi' = []$ 
// build activation graph  $\mathcal{G}'$ 
foreach  $(i, j) = e \in \mathcal{E}$  do
    if  $\phi_{i,:} \neq \mathbf{0} \vee \phi_{j,:} \neq \mathbf{0}$  then // vertex  $i$  or  $j$  is active
         $\mathcal{E}' = \mathcal{E}' \cup \{e\}$  // add edge
 $\mathcal{G}' = (\mathcal{V}, \mathcal{E}')$ 
// find connected components [30]
 $\mathcal{C} = \text{connectedComponents}(\mathcal{G}')$ 
foreach  $c \in \mathcal{C} \subset \mathcal{V}$  do // add new factor
     $\phi'_c = \mathbf{0}_{N \times 3}$ 
     $\phi'_{c,:} = \phi_{c,:}$ 
     $\Phi' = [\Phi', \text{vec}(\phi'_c)]$ 

```

Algorithm 3: Factor splitting procedure.

A.4. Parameter Random Sampling

The methods kPCA, SPCA, SSPCA, SPLOCS and ours require to set various parameters. In order to find a good parametrisation we conducted random sampling over the parameter space, where we determined reasonable ranges for the parameters experimentally.

In Table 1 the assumed distributions of the parameters for each method are summarised, where $\mathcal{U}(a, b)$ denotes the uniform distribution with the open interval (a, b) as support, $\mathcal{N}(\mu, \sigma^2)$ denotes the normal distribution with mean μ and variance σ^2 , $10^{\mathcal{U}(\cdot, \cdot)}$ is a distribution of the random variable $y = 10^x$, where $x \sim \mathcal{U}(\cdot, \cdot)$, and \bar{d}_{\max} denotes the largest distance between all pairs of vertices of the mean shape \bar{X} .

Method	Parameter Distribution
kPCA	$\beta \sim (\mathcal{U}(1, 10))^{-1}$
SPCA	$\lambda \sim \frac{1}{3N} 10^{\mathcal{U}(-4, -3)}$ (see eq. (2) in [18])
SSPCA	$\lambda \sim \frac{1}{N} 10^{\mathcal{U}(-4, -3)}$ (see eq. (2) in [18])
SPLOCS	$\lambda \sim (3K) \cdot 10^{\mathcal{U}(-4, -3)}$; $d_{\min} \sim c-w$; $d_{\max} \sim c+w$ (see eq. (6) in [23]), where $c \sim \mathcal{U}(0.1, \bar{d}_{\max} - 0.1)$ and $w \sim \mathcal{U}(0, \min(c - 0.1 , \bar{d}_{\max} - 0.1 - c))$
our	$\beta \sim (\mathcal{U}(1, 10))^{-1}$; $\lambda \sim \frac{3NK}{M} \max(10^{-8}, \mathcal{N}(64, 25))$; $\lambda_{\mathcal{G}} \sim (3 \mathcal{E})^{-0.5} \cdot 10^{\mathcal{U}(-2, 1)}$; $\lambda_1 \sim (3N)^{-0.5} \cdot 10^{\mathcal{U}(-2, 1)}$; $\lambda_2 \sim (3N)^{-0.5} \cdot 10^{\mathcal{U}(-2, 1)}$; $\lambda_{\infty} \sim 2N^{-0.5} \cdot 10^{\mathcal{U}(-2, 1)}$; $\lambda_A \sim K^{-0.5} \cdot 10^{\mathcal{U}(-5, 2)}$

Table 1. Assumed distributions of the parameters interpreted as random variables.

For each of the n_r random draws (we set $n_r = 500$ for the brain shapes dataset, and $n_r = 50$ for the human body shapes, due to the large size of the dataset), we compute the 8 scores described in section 3.1 and store them in the score matrix $\mathbf{S} \in \mathbb{R}^{n_r \times 8}$. After (linearly) mapping each n_r -dimensional column vector in \mathbf{S} onto the interval $[0, 1]$, the best parametrisation is determined by finding the index of the smallest value of the vector $\mathbf{S}\mathbf{1}_8 \in \mathbb{R}^{n_r}$.